

BridgeShape: Latent Diffusion Schrödinger Bridge for 3D Shape Completion

Dequan Kong, Zhe Zhu, Honghua Chen[†], Mingqiang Wei[†]
Nanjing University of Aeronautics and Astronautics

dqkong@nuaa.edu.com; zhuzhe0619@nuaa.edu.com; chen honghua.cn@gmail.com; mqwei@nuaa.edu.cn

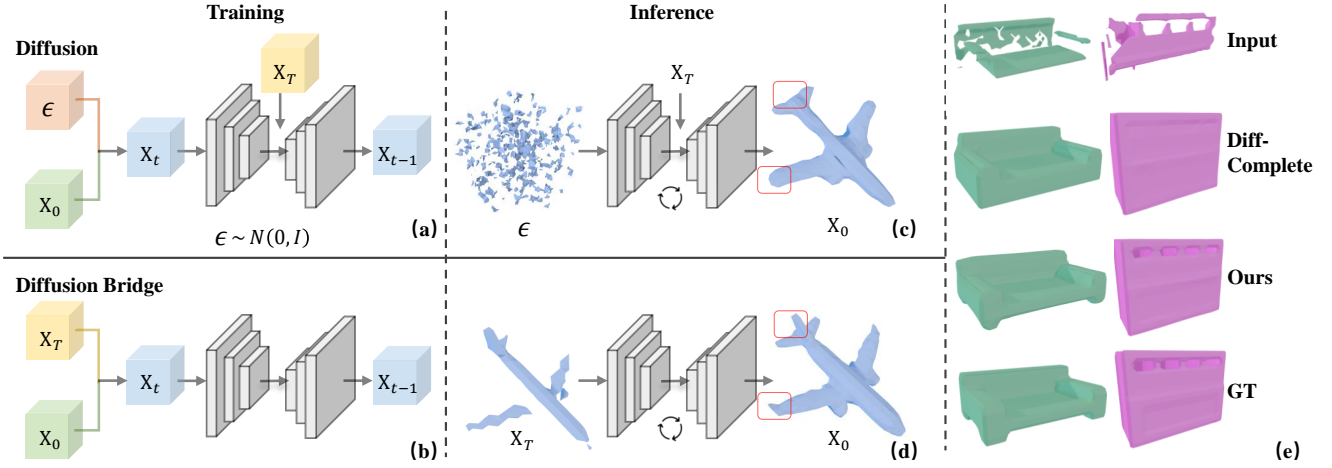


Figure 1. Comparison between existing diffusion-based shape completion paradigms and our proposed diffusion-bridge-based approach. (a) Existing diffusion models incorporate an additional branch to inject deep features into the denoising process, transmitting incomplete shape information without explicitly modeling the transformation between the incomplete shape X_T and the complete shape X_0 . (b) The proposed diffusion bridge explicitly models the optimal transport path between the distributions of incomplete and complete shapes. (c) Existing diffusion frameworks often produce less coherent completions with missing details, whereas (d) our diffusion bridge generates more structurally consistent and detailed 3D shapes. (e) Qualitative comparison of our BridgeShape with DiffComplete [12].

Abstract

Existing diffusion-based 3D shape completion methods typically use a conditional paradigm, injecting incomplete shape information into the denoising network via deep feature interactions (e.g., concatenation, cross-attention) to guide sampling toward complete shapes, often represented by voxel-based distance functions. However, these approaches fail to explicitly model the optimal global transport path, leading to suboptimal completions. Moreover, performing diffusion directly in voxel space imposes resolution constraints, limiting the generation of fine-grained geometric details. To address these challenges, we propose BridgeShape, a novel framework for 3D shape completion via latent diffusion Schrödinger bridge. The key innovations lie in two aspects: (i) BridgeShape formulates shape completion as an optimal transport problem, explicitly model-

ing the transition between incomplete and complete shapes to ensure a globally coherent transformation. (ii) We introduce a Depth-Enhanced Vector Quantized Variational Autoencoder (VQ-VAE) to encode 3D shapes into a compact latent space, leveraging self-projected multi-view depth information enriched with strong DINOv2 features to enhance geometric structural perception. By operating in a compact yet structurally informative latent space, BridgeShape effectively mitigates resolution constraints and enables more efficient and high-fidelity 3D shape completion. BridgeShape achieves state-of-the-art performance on large-scale 3D shape completion benchmarks, demonstrating superior fidelity at higher resolutions and for unseen object classes.

1. Introduction

With the rapid advancement of 3D acquisition technologies, 3D sensors have become increasingly accessible and afford-

[†]Co-corresponding authors

able, including various LiDAR scanners deployed across different platforms and RGB-D cameras such as Microsoft Kinect and Intel RealSense. This accessibility has broadened their applications in content creation, mixed reality, and machine vision [12, 52]. However, 3D sensors remain constrained by occlusions and limited angular sensing ranges, often producing fragmented and incomplete 3D scans. These limitations pose challenges for downstream applications that require complete, high-quality 3D models, necessitating shape completion techniques to faithfully recover missing geometric structures.

Early methods for 3D shape completion primarily employ convolutional neural networks [15, 19] or transformer-based architectures [33] to infer complete shapes directly from partial inputs. Subsequently, generative models, such as variational autoencoders [27, 40, 46] and adversarial networks [36, 45, 49], were explored as alternatives. More recently, diffusion probabilistic models [20, 37] have emerged as a powerful generative framework, achieving state-of-the-art results across various domains [29, 32, 35]. Building on these successes, recent works [9, 11, 12, 28] have extended diffusion models to 3D shape completion, adopting a conditional generation paradigm where incomplete shapes are injected into denoising networks via deep feature interactions (e.g., concatenation and cross-attention) to guide sampling toward complete shapes. However, most of these methods operate diffusion directly in voxel space, inherently limiting the resolution of generated shapes and restricting the ability to capture fine-grained geometric details.

Beyond resolution constraints, another fundamental limitation of diffusion-based methods is that their reverse processes always begin from Gaussian noise, which carries minimal information about the target distribution. As a result, the substantial discrepancy between the Gaussian prior and the target shape distribution necessitates additional conditioning mechanisms and more sampling steps to converge to the target distribution. Yet, these implicit strategies fail to model an optimal global transport path, ultimately hindering the accurate inference of missing geometric structures and details (see Figure 1 (c) and (e)).

In this work, we aim to address this challenge by introducing a new paradigm. Since 3D shape completion fundamentally involves modeling the optimal transport between the distributions of incomplete and complete shapes, a natural approach is to initiate the generation process directly from the given incomplete shapes, which provide a significantly more informative prior than pure noise. Fortunately, diffusion bridge models [22, 23] offer a promising solution by employing a specialized diffusion process conditioned on given endpoints, explicitly modeling the optimal transport between two distributions. While recent advances such as I²SB [23] have demonstrated the potential of diffusion bridges, their application to 3D shape completion remains

largely unexplored.

We propose BridgeShape, a novel framework for 3D shape completion via the latent diffusion Schrödinger bridge. First, to address the computational challenges inherent in 3D representations, we introduce a Depth-Enhanced VQ-VAE [42] that compresses 3D shapes into a compact yet structurally informative latent space. This representation integrates self-projected multi-view depth information enriched with strong DINOv2 [30] features, enhancing its geometric structural perception. Then, within the latent space, we construct a diffusion Schrödinger bridge between the distributions of incomplete and complete shapes, explicitly modeling the optimal transport to ensure a globally coherent transformation. By leveraging this enriched latent representation and explicit transport formulation, BridgeShape captures fine-grained geometric details and achieves high-fidelity shape completions. Extensive experiments on large-scale 3D shape completion benchmarks demonstrate state-of-the-art performance, even when generalizing to unseen object categories and higher resolutions.

Our main contributions are as follows:

- We propose BridgeShape, a novel framework for 3D shape completion that models the optimal transport between incomplete and complete shapes via a latent diffusion Schrödinger bridge.
- We introduce a Depth-Enhanced VQ-VAE to encode 3D shapes into a compact latent space, leveraging self-projected multi-view depth information enriched with strong DINOv2 features to enhance geometric structural perception.
- Extensive experiments on large-scale 3D shape completion benchmarks demonstrate that BridgeShape achieves impressive performance, delivering high-fidelity completions even at higher resolutions and on previously unseen object classes.

2. Related Work

3D Shape Completion 3D shape completion aims to recover missing regions in reconstructed shapes, playing a critical role in 3D scene understanding and modeling. Early learning-based fitting methods [15, 19] primarily rely on convolutional neural networks (CNNs) to predict complete shapes, while more recent approaches leverage transformer-based architectures [33]. For instance, 3D-EPN [15] employs a 3D encoder-decoder framework to infer complete shapes from partial volumetric inputs, while Scan2Mesh [13] optimizes a generative mesh formulation to reconstruct high-fidelity surfaces from range scans. More recently, PatchComplete [33] incorporates multi-resolution patch priors, improving generalization to unseen categories by capturing shared structures.

Beyond deterministic approaches, generative models such as GANs [36, 45, 49] and autoencoders [27, 40, 46]

have been explored for probabilistic shape completion. cGAN [45] distills the ambiguity by conditioning the completion on a learned multimodal distribution of possible results, while ShapeFormer [46] completes shapes by generating complete sequences, conditioned on the sequence for partial observation. Distinctively, we formulate a novel diffusion bridge model for 3D shape completion, explicitly modeling the transition between incomplete and complete shapes in a compact latent space enhanced by self-projected multi-view depth maps, and progressively refining the detailed latent representation of complete shapes to ensure precise and coherent results.

Diffusion models for 3D generation Diffusion models [17, 35, 37, 39] have emerged as a powerful tool for 3D shape generation, providing superior sample quality compared to GANs, while retaining the probabilistic rigor of VAEs. Recent studies [26, 41, 51] have extended diffusion models to point cloud generation, demonstrating their ability to learn complex geometric distributions. For conditional shape completion, methods such as SDFusion [9] and Diffusion-SDF [11] employ diffusion models to synthesize missing regions, typically training on synthetically cropped 3D shapes. Unlike these methods, our approach does not impose strict assumptions on the partial input, accommodating diverse levels of noise and incompleteness. Another approach, DiffComplete [12], adopts a multi-level aggregation strategy to improve completion quality. However, performing diffusion directly in voxel space requires substantial memory at higher resolutions. While scaling techniques such as gradient accumulation can mitigate this, they incur extra training complexity. However, a common limitation of these methods is their inability to explicitly model the optimal transport path between incomplete and complete shapes, often leading to suboptimal completions. BridgeShape overcomes this issue by directly modeling the optimal transport process within a compact yet structurally informative latent space, thereby enabling higher-fidelity completions while alleviating resolution constraints.

Diffusion Bridge Models Stochastic bridge models, which capture the evolution of stochastic processes constrained by fixed endpoints, have become an essential tool in probability theory [1, 6, 7]. When integrated with diffusion models, they offer a novel approach for translating between distributions and modeling conditional probabilities without relying on prior information. This data-to-data generation paradigm has attracted significant interest in various generative tasks, including image-to-image translation [5, 16, 22, 23], protein matching [38], point cloud denoising [43], and text-to-speech synthesis [8]. However, despite these promising advances, the application of diffusion bridge models to 3D shape completion remains largely

unexplored. Our work aims to bridge this gap.

3. Method

3.1. Overview

The overall architecture of our approach is exhibited in Figure 2. Given a partial scan and its corresponding ground truth complete shape, following previous practice [12], we represent the partial scan as a truncated signed distance field (TSDF) and the complete shape as a truncated unsigned distance field (TUDF) in a volumetric grid. To accelerate the diffusion-based completion framework, we first compress the complete shape into a low-resolution latent space using a VQ-VAE [9, 34, 42] enhanced by multi-view depth information (Section 3.2). Built upon the pretrained latent shape space, the diffusion Schrödinger bridge [23] is utilized to model the diffusion process from the partial to the complete shape (Section 3.3).

3.2. 3D Shape Compression

VQ-VAE Compression The VQ-VAE consists of an encoder \mathcal{E}_c that maps a 3D shape into a latent space, and a decoder \mathcal{D} that reconstructs the shape from the latent vector. This architecture enables the application of diffusion models by providing a compact, lower-dimensional representation of the shape.

Let $\mathbf{X} \in \mathbb{R}^{D \times D \times D}$ represent a complete 3D shape in the form of a TUDF. The encoder \mathcal{E}_c maps this shape to a latent vector $\mathbf{z} \in \mathbb{R}^{d \times d \times d}$, where $d < D$:

$$\mathbf{z} = \mathcal{E}_c(\mathbf{X}) \quad (1)$$

the latent vector \mathbf{z} is then quantized by selecting the closest codebook element Z :

$$\mathcal{VQ}(\mathbf{z}) = \arg \min_{\mathbf{z}_i \in Z} \|\mathbf{z} - \mathbf{z}_i\|_2 \quad (2)$$

where $\mathbf{z}_i \in Z$ represents an element from the codebook, and $\|\cdot\|_2$ denotes the L2 norm. The decoder \mathcal{D} reconstructs the shape from \mathbf{z} defined as:

$$\mathbf{X}' = \mathcal{D}(\mathcal{VQ}(\mathbf{z})). \quad (3)$$

The encoder, decoder, and codebook are jointly optimized with the following total loss function:

$$\mathcal{L}_{\text{total}} = -\log p(\mathbf{X} | \mathbf{z}) + \|\hat{\mathbf{z}} - \text{sg}[\mathbf{z}]\|^2 + \|\text{sg}[\hat{\mathbf{z}}] - \mathbf{z}\|^2 \quad (4)$$

where $\text{sg}[\cdot]$ is the stop-gradient operation. The three terms in Equation 4 are: the reconstruction loss, the commitment loss, and the VQ objective.

Enhancement with Multi-View Depth Features To strengthen the latent space representation, we incorporate

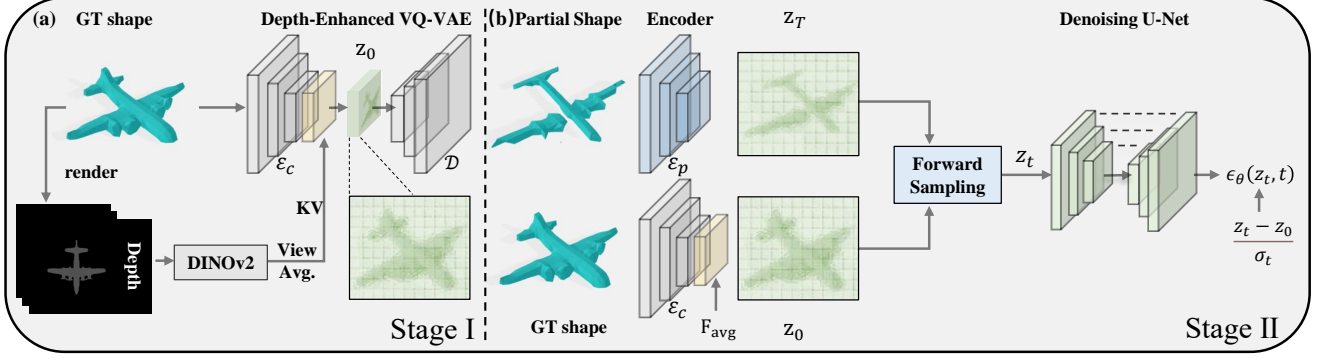


Figure 2. Overview of our training pipeline, which operates within the latent space based on the diffusion Schrödinger bridge. **Stage I:** Pre-training a Depth-Enhanced VQ-VAE on complete shapes to establish the latent space. **Stage II:** A co-trained encoder maps partial TSDF inputs into this latent space, where the diffusion bridge is applied to learn a structured diffusion trajectory between incomplete and complete shapes. This approach significantly enhances both efficiency and fidelity in shape completion.

multi-view depth features into the VQ-VAE. Specifically, we project the 3D shape into depth maps from N viewpoints, where each depth map is denoted as \mathbf{D}_i for the i -th view, and its corresponding feature \mathbf{F}_i is extracted using a pre-trained DINOv2 model [30]. To obtain a unified representation, we aggregate these features by averaging along the view dimension as a simple yet effective fusion strategy:

$$\mathbf{F}_{avg} = \frac{1}{N} \sum_{i=1}^N \mathbf{F}_i.$$

This operation produces an aggregated feature map \mathbf{F}_{avg} that fuses complementary information across all viewpoints while minimizing redundant details, resulting in a robust representation with minimal computational overhead. \mathbf{F}_{avg} is then fused with the 3D shape’s latent feature via a cross-attention mechanism at the end of the encoder \mathcal{E}_c . In this fusion process, the query matrix is derived from the 3D shape’s latent feature, while the key and value matrix are derived from \mathbf{F}_{avg} . This fusion is performed at a critical stage—the end of the encoder—where the shape information has already been compressed into a high-level representation. This approach strikes a balance between model performance and resource utilization, avoiding unnecessary overhead while enriching the latent space representation.

3.3. Latent Diffusion Schrödinger Bridge

After compressing complete 3D shapes into a high-dimensional latent space, we construct a diffusion Schrödinger bridge to model the optimal transport between incomplete and complete shapes. As illustrated in Figure 2(b), we freeze the pre-trained VQ-VAE parameters and employ an additional trainable encoder, \mathcal{E}_p , to map partial inputs into the same latent space, where the latent representations of a given incomplete shape and its corresponding complete shape are denoted by \mathbf{z}_T and \mathbf{z}_0 , respec-

tively. Then, the diffusion bridge enables efficient processing within this compact yet structurally informative space. In the following, we detail how 3D shape completion is formulated as an optimal transport problem via the diffusion bridge and provide an overview of the associated training and inference procedures.

Optimal Transport via Diffusion Schrödinger Bridge

Diffusion Schrödinger bridge is a specialized diffusion process that progressively transforms $\mathbf{z}_0 \sim p_A$ into $\mathbf{z}_T \sim p_B$ via a sequence of intermediate states $\{\mathbf{z}_1, \dots, \mathbf{z}_T\}$ over T timesteps.

Given a reference path measure $\pi(\mathbf{z}_{0:T})$ that characterizes the ideal diffusion trajectory, our goal is to learn a process $p^*(\mathbf{z}_{0:T})$ that satisfies $p^*(\mathbf{z}_0) = p_A$ and $p^*(\mathbf{z}_T) = p_B$, while minimizing the Kullback-Leibler divergence between $\pi(\mathbf{z}_{0:T})$ and $p^*(\mathbf{z}_{0:T})$. This formulation is equivalent to the Schrödinger Bridge problem [8, 21, 43], whose dynamics are characterized by the following stochastic differential equations (SDEs):

$$d\mathbf{z}_t = [\mathbf{f}(\mathbf{z}_t, t) + g^2(t)\nabla \log \Psi_t(\mathbf{z}_t)] dt + g(t) d\mathbf{w}_t, \quad (5)$$

$$d\mathbf{z}_t = [\mathbf{f}(\mathbf{z}_t, t) - g^2(t)\nabla \log \hat{\Psi}_t(\mathbf{z}_t)] dt + g(t) d\bar{\mathbf{w}}_t, \quad (6)$$

where $\mathbf{f}(\mathbf{z}_t, t)$ is the drift term, $g(t)$ is the diffusion coefficient and \mathbf{w}_t is a Wiener process. The terms $\nabla \log \Psi_t(\mathbf{z}_t)$ and $\nabla \log \hat{\Psi}_t(\mathbf{z}_t)$ represent the extra nonlinear drift terms that solve the coupled partial differential equations (PDEs):

$$\begin{cases} \frac{\partial \Psi}{\partial t} = -\nabla \Psi^T \mathbf{f} - \frac{1}{2} \text{Tr}(g^2 \nabla^2 \Psi) \\ \frac{\partial \hat{\Psi}}{\partial t} = -\nabla(\hat{\Psi} \mathbf{f}) + \frac{1}{2} \text{Tr}(g^2 \nabla^2 \hat{\Psi}) \end{cases} \quad (7)$$

such that

$$\Psi_0 \hat{\Psi}_0 = p_A, \quad \Psi_T \hat{\Psi}_T = p_B. \quad (8)$$

However, directly solving the Schrödinger bridge formulation is computationally prohibitive. To mitigate it, we leverage a framework from recent works [8, 23, 43] under the assumption that paired training data is available, i.e.,

$$p(\mathbf{z}_0, \mathbf{z}_T) = p_A(\mathbf{z}_0) p_B(\mathbf{z}_T | \mathbf{z}_0).$$

In the context of 3D shape completion, the latent distribution over incomplete shapes is modeled by a joint distribution: $p_A(\mathbf{z}_0)$ represents the latent distribution of complete shapes, and $p_B(\mathbf{z}_T | \mathbf{z}_0)$ characterizes the latent distribution of missing components conditioned on the complete shapes.

Given a boundary pair \mathbf{z}_0 (complete shape) and \mathbf{z}_T (incomplete shape), and assuming $\mathbf{f} := 0$, the posterior distribution at each timestep t is defined as:

$$q(\mathbf{z}_t | \mathbf{z}_0, \mathbf{z}_T) = \mathcal{N}(\mathbf{z}_t; \mu_t(\mathbf{z}_0, \mathbf{z}_T), \Sigma_t), \quad (9)$$

where the mean μ_t and covariance Σ_t are computed as:

$$\mu_t(\mathbf{z}_0, \mathbf{z}_T) = \frac{\sigma_{b,t}^2}{\sigma_{b,t}^2 + \sigma_t^2} \mathbf{z}_0 + \frac{\sigma_t^2}{\sigma_{b,t}^2 + \sigma_t^2} \mathbf{z}_T, \quad (10)$$

$$\Sigma_t = \frac{\sigma_t^2 \sigma_{b,t}^2}{\sigma_t^2 + \sigma_{b,t}^2}. \quad (11)$$

Here, σ_t^2 and $\sigma_{b,t}^2$ represent the accumulated variance from \mathbf{z}_T and \mathbf{z}_0 , respectively. This framework enables efficient computation of the coupled PDEs (see Equation 7), thereby facilitating the latent space diffusion process. Moreover, the sampling mechanism in Equation 9 is both tractable and sufficiently expressive to cover the generative trajectory, resulting in an effective and efficient shape completion pipeline.

Considering that extremely sparse incomplete shapes can introduce significant uncertainty in the missing regions, establishing a robust optimal transport path may become particularly challenging. To address this, we inject stochasticity into the latent distribution of incomplete shapes before constructing the optimal transport process—following the strategy employed in [23]. A detailed analysis of this approach is presented in our ablation study (Section 4.4).

Noise Prediction and Inference Our training objective is to accurately predict the noise injected at each timestep during the forward diffusion process. This is accomplished using a neural network ϵ_θ that estimates the noise $\epsilon_\theta(\mathbf{z}_t, t)$ at every timestep t . The training loss is defined as:

$$\mathcal{L} = \|\epsilon_\theta(\mathbf{z}_t, t) - \frac{\mathbf{z}_t - \mathbf{z}_0}{\sigma_t}\|_2^2. \quad (12)$$

During inference, we can run standard DDPM [20] to iteratively refine the complete shape’s latent representation, starting from \mathbf{z}_T (the latent code of the incomplete

shape) and using reverse dynamics governed by the mean $\mu_t(\hat{\mathbf{z}}_0, \mathbf{z}_T)$ and covariance Σ_t as:

$$p(\mathbf{z}_{t-1} | \mathbf{z}_t, \hat{\mathbf{z}}_0) = \mathcal{N}(\mathbf{z}_{t-1}; \mu_t(\hat{\mathbf{z}}_0, \mathbf{z}_T), \Sigma_t). \quad (13)$$

This induces the same marginal density of Schrödinger bridge paths when $\hat{\mathbf{z}}_0$ is closed to \mathbf{z}_0 [23, 43].

4. Experiments

4.1. Experimental Settings

Datasets We evaluate our method on two large-scale shape completion benchmarks: 3D-EPN [15] and PatchComplete [33]. The 3D-EPN dataset contains 25,590 training and 5,384 testing object instances, all from 8 ShapeNet categories [4]. Each object has six partial scans with varying completeness, represented as 32^3 TSDF grids, resulting in 153,540 training samples. The complete shapes are represented as 32^3 or 64^3 TUDFs. These partial scans are generated via virtual scanning using depth maps, backprojected into a shared volumetric grid. Ground truth shapes are obtained through a distance field transform [2]. The PatchComplete dataset includes synthetic ShapeNet data and real-world scan data from ScanNet [14], focusing on shape completion from unseen categories. For ShapeNet, 18 categories are used for training and 8 for testing, with 3,202 training models and 1,325 test models, each having four partial scans. The ScanNet data consists of objects extracted from bounding boxes, with complete shapes provided by Scan2CAD [3]. All objects are represented as 32^3 TSDF units, with truncation values of 2.5 voxel units for ShapeNet and 3 voxels for ScanNet. These datasets allow us to evaluate our method on both synthetic and real-world data, testing its ability to handle unseen categories and varying levels of completeness.

Evaluation We evaluate our method using standard metrics for shape completion. On the 3D-EPN dataset [15], we report the mean l_1 error across all voxels of the TUDF predictions. For PatchComplete benchmark [33], we use the l_1 Chamfer Distance (CD) and Intersection over Union (IoU) to evaluate the geometry of predicted shapes. 10K points are sampled on surfaces for CD calculation.

4.2. Evaluation on known object categories

The quantitative and qualitative comparison with state-of-the-art methods [12, 15, 27, 31, 33, 46, 48, 50] on the 3D-EPN dataset [15] is presented in Table 1 and Figure 3. For the probabilistic methods [12, 27, 48], we report the average results across five inferences with different initializations. In comparison to the second-ranked method DiffComplete [12], BridgeShape reduces the L1 error by approximately 26% (from 0.053 to 0.039), while producing high-fidelity, realistic shapes with fewer surface artifacts. This

Table 1. Quantitative comparison for shape completion on objects of known categories [15].

| l_1 -err. (\downarrow) | Chair | Table | Sofa | Lamp | Plane | Car | Dresser | Watercraft | Avg. |
|------------------------------|--------------|--------------|--------------|--------------|--------------|--------------|--------------|--------------|--------------|
| 3D-EPN [15] | 0.418 | 0.377 | 0.392 | 0.388 | 0.421 | 0.259 | 0.381 | 0.356 | 0.374 |
| ConvONet [31] | 0.210 | 0.247 | 0.254 | 0.234 | 0.185 | 0.195 | 0.250 | 0.184 | 0.220 |
| SDF-StyleGAN [50] | 0.321 | 0.256 | 0.289 | 0.280 | 0.295 | 0.224 | 0.273 | 0.282 | 0.278 |
| cGCA [48] | 0.174 | 0.212 | 0.179 | 0.239 | 0.170 | 0.161 | 0.204 | 0.143 | 0.185 |
| AutoSDF [27] | 0.201 | 0.258 | 0.226 | 0.275 | 0.184 | 0.187 | 0.248 | 0.157 | 0.217 |
| ShapeFormer [46] | 0.104 | 0.175 | 0.133 | 0.176 | 0.136 | 0.127 | 0.157 | 0.119 | 0.141 |
| PatchComplete [33] | 0.134 | 0.095 | 0.084 | 0.087 | 0.061 | 0.053 | 0.134 | 0.058 | 0.088 |
| Diffcomplete [12] | 0.070 | 0.073 | 0.061 | 0.059 | 0.015 | 0.025 | 0.086 | 0.031 | 0.053 |
| BridgeShape (Ours) | 0.055 | 0.059 | 0.047 | 0.038 | 0.012 | 0.023 | 0.055 | 0.022 | 0.039 |

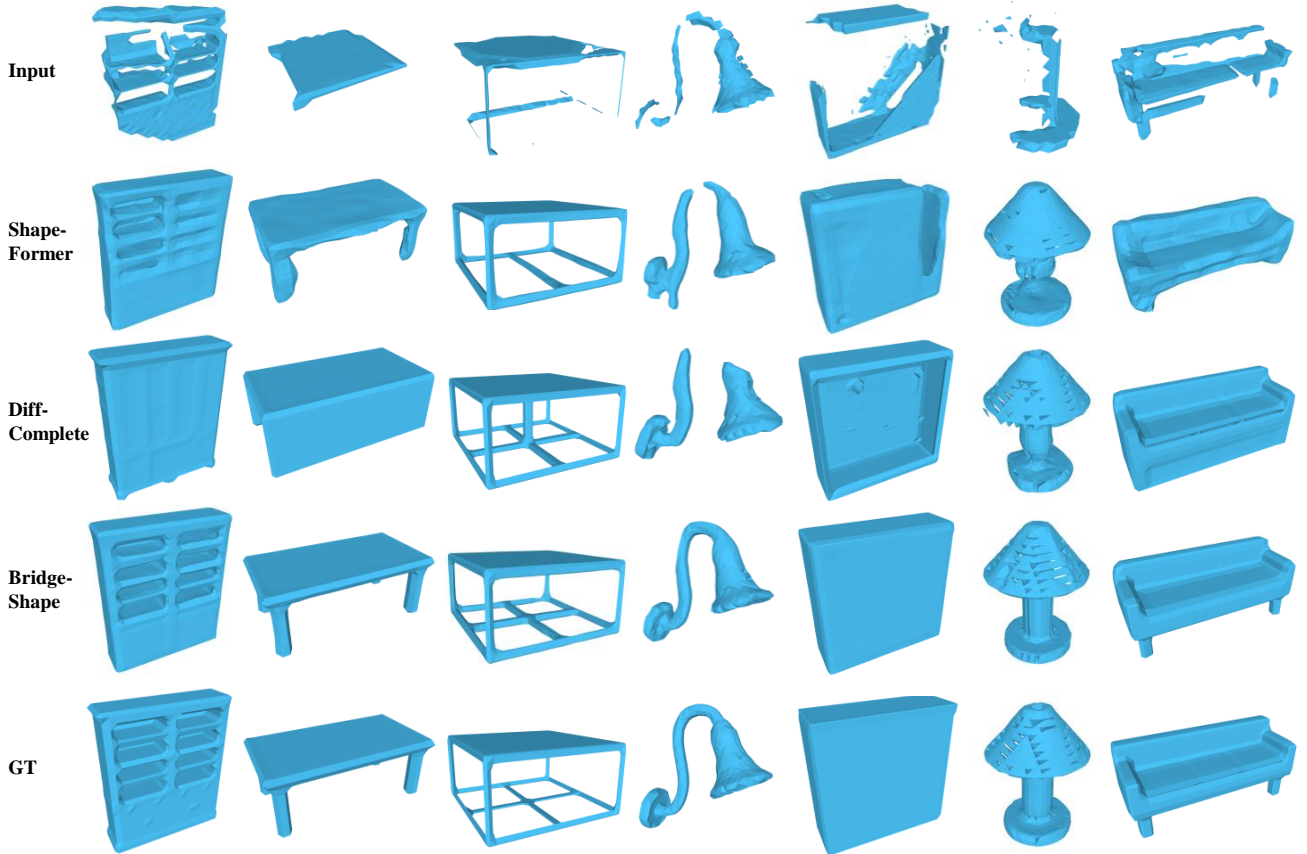


Figure 3. Qualitative comparison of shape completion on 3D-EPN [15].

is because DiffComplete reverses from unstructured Gaussian noise and relies on deep feature interactions to inject incomplete shape information, while our approach directly starts the generation process from the input incomplete shapes, providing a far more informative prior. Additionally, compared to GAN-based SDF-StyleGAN [50], autoregressive methods AutoSDF [27] and ShapeFormer [46], our diffusion bridge-based generative model exhibits enhanced mode coverage and superior sampling quality. Moreover, while deterministic approaches [15, 31, 33] perform one-

step mappings, BridgeShape refines shapes iteratively during the diffusion bridge process, significantly enhancing accuracy and reducing artifacts.

4.3. Evaluation on Unseen Object Categories

To assess BridgeShape’s generalization capabilities, we evaluate its performance on unseen object categories from both synthetic ShapeNet [4] and real-world ScanNet data [14]. As shown in Table 2 and Table 3, BridgeShape excels in handling unseen categories, outperforming state-

Table 2. Quantitative comparison for shape completion on synthetic objects [4] of unseen categories. ($CD \times 10^2$ and $IoU \times 10^2$)

| | Bag | | Lamp | | Bathtub | | Bed | | Basket | | Printer | | Laptop | | Bench | | Avg. | |
|--------------------|-------------|-------------|-------------|-------------|-------------|-------------|-------------|-------------|-------------|-------------|-------------|-------------|-------------|-------------|-------------|-------------|-------------|-------------|
| | CD | IoU | CD | IoU | CD | IoU | CD | IoU | CD | IoU | CD | IoU | CD | IoU | CD | IoU | CD | IoU |
| 3D-EPN [15] | 5.01 | 73.8 | 8.07 | 47.2 | 4.21 | 57.9 | 5.84 | 58.4 | 7.90 | 54.0 | 5.15 | 73.6 | 3.90 | 62.0 | 4.54 | 48.3 | 5.58 | 59.4 |
| Few-Shot [44] | 8.00 | 56.1 | 15.1 | 25.4 | 7.05 | 45.7 | 10.0 | 39.6 | 8.72 | 40.6 | 9.26 | 56.7 | 10.4 | 31.3 | 8.11 | 27.2 | 9.58 | 40.3 |
| IF-Nets [10] | 4.77 | 69.8 | 5.70 | 50.8 | 4.72 | 55.0 | 5.34 | 60.7 | 4.44 | 50.2 | 5.83 | 70.5 | 6.47 | 58.3 | 5.03 | 49.7 | 5.29 | 58.1 |
| Auto-SDF [27] | 5.81 | 56.3 | 6.57 | 39.1 | 5.17 | 41.0 | 6.01 | 44.6 | 6.70 | 39.8 | 7.52 | 49.9 | 4.81 | 51.1 | 4.31 | 39.5 | 5.86 | 45.2 |
| ConvONet [31] | 5.10 | 70.8 | 5.42 | 52.6 | 4.96 | 60.4 | 5.42 | 63.2 | 6.16 | 54.6 | 5.56 | 72.1 | 4.78 | 57.3 | 4.69 | 49.6 | 5.26 | 60.1 |
| PatchComplete [33] | 3.94 | 77.6 | 4.68 | 56.4 | 3.78 | 66.3 | 4.49 | 66.8 | 5.15 | 61.0 | 4.63 | 77.6 | 3.77 | 63.8 | 3.70 | 53.9 | 4.27 | 65.4 |
| DiffComplete [12] | 3.86 | 78.3 | 4.80 | 57.9 | 3.52 | 68.9 | 4.16 | 67.1 | 4.94 | 65.5 | 4.40 | 76.8 | 3.52 | 67.4 | 3.56 | 58.2 | 4.10 | 67.5 |
| BridgeShape (Ours) | 3.70 | 80.0 | 4.94 | 62.7 | 3.41 | 69.8 | 4.32 | 69.6 | 5.50 | 65.1 | 4.09 | 81.4 | 3.13 | 72.7 | 3.38 | 59.1 | 4.06 | 70.1 |

Table 3. Quantitative comparison for shape completion on real-world objects [14] of unseen categories. ($CD \times 10^2$ and $IoU \times 10^2$)

| | Bag | | Lamp | | Bathtub | | Bed | | Basket | | Printer | | Avg. | |
|--------------------|-------------|-------------|-------------|-------------|-------------|-------------|-------------|-------------|-------------|-------------|-------------|-------------|-------------|-------------|
| | CD | IoU | CD | IoU | CD | IoU | CD | IoU | CD | IoU | CD | IoU | CD | IoU |
| 3D-EPN [15] | 8.83 | 53.7 | 14.3 | 20.7 | 7.56 | 41.0 | 7.76 | 47.8 | 7.74 | 36.5 | 8.36 | 63.0 | 9.09 | 44.0 |
| Few-Shot [44] | 9.10 | 44.9 | 11.9 | 19.6 | 7.77 | 38.2 | 9.07 | 34.9 | 8.02 | 34.3 | 8.30 | 62.2 | 9.02 | 38.6 |
| IF-Nets [10] | 8.96 | 44.2 | 10.2 | 24.9 | 7.19 | 39.5 | 8.24 | 44.9 | 6.74 | 42.7 | 8.28 | 60.7 | 8.26 | 42.6 |
| Auto-SDF [27] | 9.30 | 48.7 | 11.2 | 24.4 | 7.84 | 36.6 | 7.91 | 38.0 | 7.54 | 36.1 | 9.66 | 49.9 | 8.90 | 38.9 |
| ConvONet [31] | 9.12 | 52.5 | 9.83 | 20.3 | 7.93 | 41.2 | 8.14 | 41.6 | 7.39 | 37.0 | 7.62 | 64.9 | 8.34 | 42.9 |
| PatchComplete [33] | 8.23 | 58.3 | 9.42 | 28.4 | 6.77 | 48.0 | 7.24 | 48.4 | 6.60 | 45.5 | 6.84 | 70.5 | 7.52 | 49.8 |
| DiffComplete [12] | 7.05 | 48.5 | 6.84 | 30.5 | 8.22 | 48.5 | 7.20 | 46.6 | 7.42 | 59.2 | 6.36 | 74.5 | 7.18 | 51.3 |
| BridgeShape (Ours) | 7.67 | 61.2 | 8.07 | 36.3 | 6.28 | 50.9 | 6.87 | 51.3 | 6.20 | 50.2 | 6.83 | 71.0 | 6.99 | 53.5 |

Table 4. Ablation on different diffusion mechanisms.

| Mechanisms | l_1 -err. (\downarrow) |
|---|------------------------------|
| Conventional diffusion | 0.047 |
| Diffusion Schrödinger Bridge | 0.045 |
| Diffusion Schrödinger Bridge + Stochasticity (Ours) | 0.039 |

of-the-art methods [10, 12, 15, 27, 31, 33, 44] in terms of CD and IoU on average. This can be attributed to the fact that BridgeShape enforces globally coherent transport via the Schrödinger bridge formulation, effectively modeling shared structures among different categories. This leads to superior performance on unseen categories, including real-world scans that are typically cluttered and noisy. Figure 4 provides compelling visual evidence that BridgeShape robustly generalizes to unseen categories, producing high-fidelity completions that preserve fine geometric details on both synthetic and real-world datasets.

4.4. Ablation Studies

To understand the individual contributions of each component in BridgeShape, we conduct a series of ablation experiments on the 3D-EPN dataset [15]. Unless otherwise specified, for each experiment, we evaluate the model’s performance across all categories and report the average results.

Effects of Diffusion Schrödinger Bridge One of the key innovations in BridgeShape is the diffusion Schrödinger bridge, which explicitly models optimal transport between the latent distributions of incomplete and complete shapes. To assess its impact, we compare it with a conventional diffusion paradigm with an additional conditional branch, similar to DiffComplete [12]. However, as shown in Table 4, this approach yields suboptimal results, underscoring the importance of explicitly modeling the transport process to achieve superior shape completions. Building on this, we further investigate the effect of stochasticity on the optimal transport process. As discussed in Section 3.3, we introduce stochasticity by injecting Gaussian noise into the latent distribution of incomplete shapes before constructing the optimal transport process. To validate this design choice, we conduct an ablation study comparing completion performance with and without noise injection. As shown in Table 4, omitting this noise leads to significant performance degradation, confirming that stochasticity plays a crucial role in facilitating a robust optimal transport process. We attribute this improvement to the noise compensating for missing parts, thereby stabilizing the transport trajectory and ultimately yielding more precise shape completions. Qualitative comparison results can be found in the supplementary material.

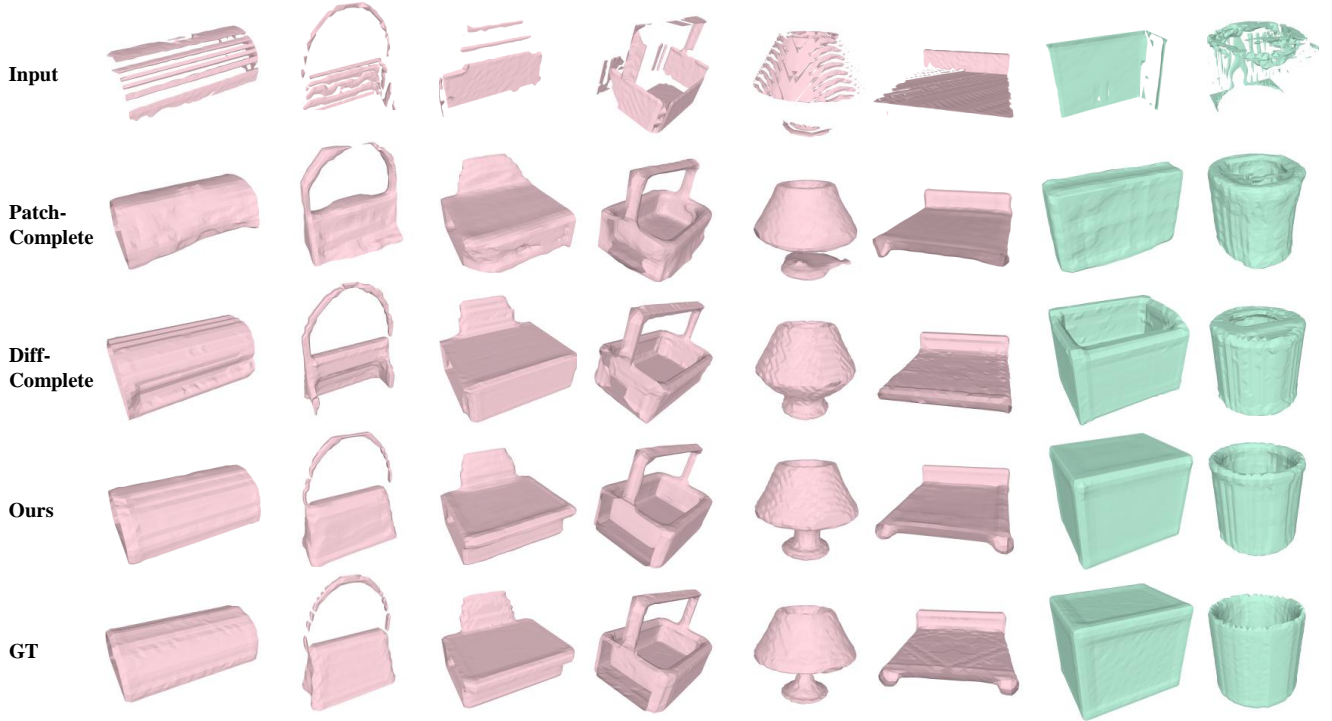


Figure 4. Qualitative comparison on the synthetic (pink) ShapeNet [4] dataset and real-world (green) ScanNet [14] dataset.

Table 5. Ablation on the effect of Depth-Enhanced VQ-VAE.

| Variants | Rec. $l_1 \downarrow$ | Comp. $l_1 \downarrow$ | Comp. IoU \uparrow |
|-----------------|-----------------------|------------------------|----------------------|
| W/o. Depth | 0.0042 | 0.041 | 92.36% |
| W. Depth (Ours) | 0.0021 | 0.039 | 94.41% |

Effects of Depth-Enhanced VQ-VAE The Depth-Enhanced VQ-VAE serves as the foundation for the diffusion Schrödinger bridge. Unlike a standard VQ-VAE [9, 34, 42], which captures a compact latent representation but struggles to retain structural details, our approach integrates self-projected multi-view depth information enriched with DINOv2 [30] features to enhance geometric perception. To assess its effectiveness, we compare it against a standard VQ-VAE without depth features. As shown in Table 5, integrating multi-view depth into our VQ-VAE halves its reconstruction l_1 error (0.0042→0.0021), yields a 0.002 reduction in completion l_1 error, and boosts IoU by $\sim 2\%$ (92.36%→94.41%). Removing depth reverses these gains, underscoring the critical role of multi-view depth. Additional ablation studies and qualitative results are provided in the supplementary material.

4.5. Results on Higher Voxel Resolution

While our primary experiments use a voxel resolution of 32^3 , we further evaluate on 3D-EPN [15] at 64^3 and 128^3 to assess scalability (Table 6). Higher resolutions enable finer-

Table 6. Quantitative results on 3D-EPN [15]. We report the detailed results under l_1 -error on 8 categories for different resolutions. Low is better.

| Categories | l_1 -err. (32^3) | l_1 -err. (64^3) | l_1 -err. (128^3) |
|------------|------------------------|------------------------|-------------------------|
| Chair | 0.055 | 0.045 | 0.044 |
| Table | 0.059 | 0.053 | 0.054 |
| Sofa | 0.047 | 0.051 | 0.050 |
| Lamp | 0.038 | 0.034 | 0.026 |
| Plane | 0.012 | 0.009 | 0.009 |
| Car | 0.023 | 0.024 | 0.024 |
| Dresser | 0.055 | 0.062 | 0.058 |
| Watercraft | 0.022 | 0.019 | 0.019 |
| Avg. | 0.039 | 0.037 | 0.036 |

grained shape completion and yield increasingly higher average accuracy. These results confirm that BridgeShape effectively leverages increased resolution to enhance completion quality. Qualitative results are provided in the supplementary material.

5. Conclusion

In this paper, we introduce BridgeShape, a novel framework for 3D shape completion based on a latent diffusion Schrödinger bridge. By leveraging a latent space enriched with multi-view depth features, BridgeShape en-

hances both efficiency and accuracy. This compact, geometrically informative representation facilitates the modeling of an optimal transport trajectory, enabling a smooth diffusion process from incomplete to complete shapes. As a result, BridgeShape ensures high-fidelity shape completion while preserving structural consistency throughout the process. Extensive experiments on large-scale 3D shape completion benchmarks demonstrate that BridgeShape achieves state-of-the-art performance, maintaining high resolution and generalizing well to unseen object categories.

References

- [1] Javier Aguilar, Joseph W Baron, Tobias Galla, and Raúl Toral. Sampling rare trajectories using stochastic bridges. *Physical Review E*, 105(6):064138, 2022. 3
- [2] John Amanatides, Andrew Woo, et al. A fast voxel traversal algorithm for ray tracing. In *Eurographics*, pages 3–10. Citeseer, 1987. 5
- [3] Armen Avetisyan, Manuel Dahnert, Angela Dai, Manolis Savva, Angel X Chang, and Matthias Nießner. Scan2cad: Learning cad model alignment in rgb-d scans. In *Proceedings of the IEEE/CVF Conference on computer vision and pattern recognition*, pages 2614–2623, 2019. 5
- [4] Angel X Chang, Thomas Funkhouser, Leonidas Guibas, Pat Hanrahan, Qixing Huang, Zimo Li, Silvio Savarese, Manolis Savva, Shuran Song, Hao Su, et al. Shapenet: An information-rich 3d model repository. *arXiv preprint arXiv:1512.03012*, 2015. 5, 6, 7, 8, 18
- [5] Tianrong Chen, Guan-Horng Liu, and Evangelos A Theodorou. Likelihood training of schrödinger bridge using forward-backward sdes theory. *arXiv preprint arXiv:2110.11291*, 2021. 3
- [6] Yongxin Chen and Tryphon Georgiou. Stochastic bridges of linear systems. *IEEE Transactions on Automatic Control*, 61(2):526–531, 2015. 3
- [7] Yongxin Chen, Tryphon T Georgiou, and Michele Pavon. Stochastic control liaisons: Richard sinkhorn meets gaspard monge on a schrodinger bridge. *Siam Review*, 63(2):249–313, 2021. 3
- [8] Zehua Chen, Guande He, Kaiwen Zheng, Xu Tan, and Jun Zhu. Schrodinger bridges beat diffusion models on text-to-speech synthesis. *arXiv preprint arXiv:2312.03491*, 2023. 3, 4, 5
- [9] Yen-Chi Cheng, Hsin-Ying Lee, Sergey Tulyakov, Alexander G Schwing, and Liang-Yan Gui. Sdfusion: Multimodal 3d shape completion, reconstruction, and generation. In *Proceedings of the IEEE/CVF conference on computer vision and pattern recognition*, pages 4456–4465, 2023. 2, 3, 8
- [10] Julian Chibane, Thiemo Alldieck, and Gerard Pons-Moll. Implicit functions in feature space for 3d shape reconstruction and completion. In *Proceedings of the IEEE/CVF conference on computer vision and pattern recognition*, pages 6970–6981, 2020. 7
- [11] Gene Chou, Yuval Bahat, and Felix Heide. Diffusion-sdf: Conditional generative modeling of signed distance functions. In *Proceedings of the IEEE/CVF international conference on computer vision*, pages 2262–2272, 2023. 2, 3
- [12] Ruihang Chu, Enze Xie, Shentong Mo, Zhenguo Li, Matthias Nießner, Chi-Wing Fu, and Jiaya Jia. Diffcomplete: Diffusion-based generative 3d shape completion. *Advances in Neural Information Processing Systems*, 36, 2024. 1, 2, 3, 5, 6, 7, 14, 15, 16, 17, 18, 19
- [13] Angela Dai and Matthias Nießner. Scan2mesh: From unstructured range scans to 3d meshes. In *Proceedings of the IEEE/CVF Conference on Computer Vision and Pattern Recognition*, pages 5574–5583, 2019. 2
- [14] Angela Dai, Angel X Chang, Manolis Savva, Maciej Halber, Thomas Funkhouser, and Matthias Nießner. Scannet: Richly-annotated 3d reconstructions of indoor scenes. In *Proceedings of the IEEE conference on computer vision and pattern recognition*, pages 5828–5839, 2017. 5, 6, 7, 8, 19
- [15] Angela Dai, Charles Ruizhongtai Qi, and Matthias Nießner. Shape completion using 3d-encoder-predictor cnns and shape synthesis. In *Proceedings of the IEEE conference on computer vision and pattern recognition*, pages 5868–5877, 2017. 2, 5, 6, 7, 8, 12, 13, 14, 15, 17
- [16] Valentin De Bortoli, James Thornton, Jeremy Heng, and Arnaud Doucet. Diffusion schrödinger bridge with applications to score-based generative modeling. *Advances in Neural Information Processing Systems*, 34:17695–17709, 2021. 3
- [17] Prafulla Dhariwal and Alexander Nichol. Diffusion models beat gans on image synthesis. *Advances in neural information processing systems*, 34:8780–8794, 2021. 3
- [18] P Kingma Diederik. Adam: A method for stochastic optimization. (*No Title*), 2014. 12
- [19] Xiaoguang Han, Zhen Li, Haibin Huang, Evangelos Kalogerakis, and Yizhou Yu. High-resolution shape completion using deep neural networks for global structure and local geometry inference. In *Proceedings of the IEEE international conference on computer vision*, pages 85–93, 2017. 2
- [20] Jonathan Ho, Ajay Jain, and Pieter Abbeel. Denoising diffusion probabilistic models. *Advances in neural information processing systems*, 33:6840–6851, 2020. 2, 5
- [21] Christian Léonard. A survey of the schrödinger problem and some of its connections with optimal transport. *arXiv preprint arXiv:1308.0215*, 2013. 4
- [22] Bo Li, Kaitao Xue, Bin Liu, and Yu-Kun Lai. Bbmd: Image-to-image translation with brownian bridge diffusion models. In *Proceedings of the IEEE/CVF conference on computer vision and pattern Recognition*, pages 1952–1961, 2023. 2, 3
- [23] Guan-Horng Liu, Arash Vahdat, De-An Huang, Evangelos A Theodorou, Weili Nie, and Anima Anandkumar. I²sb: Image-to-image schrödinger bridge. *arXiv preprint arXiv:2302.05872*, 2023. 2, 3, 5
- [24] William E Lorensen and Harvey E Cline. Marching cubes: A high resolution 3d surface construction algorithm. *ACM SIGGRAPH Computer Graphics*, 21(4):163–169, 1987. 12
- [25] I Loshchilov. Decoupled weight decay regularization. *arXiv preprint arXiv:1711.05101*, 2017. 12

- [26] Shitong Luo and Wei Hu. Diffusion probabilistic models for 3d point cloud generation. In *Proceedings of the IEEE/CVF conference on computer vision and pattern recognition*, pages 2837–2845, 2021. 3
- [27] Paritosh Mittal, Yen-Chi Cheng, Maneesh Singh, and Shubham Tulsiani. Autosdf: Shape priors for 3d completion, reconstruction and generation. In *Proceedings of the IEEE/CVF Conference on Computer Vision and Pattern Recognition*, pages 306–315, 2022. 2, 5, 6, 7
- [28] Norman Müller, Yawar Siddiqui, Lorenzo Porzi, Samuel Rota Bulo, Peter Kotschieder, and Matthias Nießner. Diffirf: Rendering-guided 3d radiance field diffusion. In *Proceedings of the IEEE/CVF Conference on Computer Vision and Pattern Recognition*, pages 4328–4338, 2023. 2
- [29] Alexander Quinn Nichol and Prafulla Dhariwal. Improved denoising diffusion probabilistic models. In *International conference on machine learning*, pages 8162–8171. PMLR, 2021. 2
- [30] Maxime Oquab, Timothée Darcet, Théo Moutakanni, Huy Vo, Marc Szafranec, Vasil Khalidov, Pierre Fernandez, Daniel Haziza, Francisco Massa, Alaaeldin El-Nouby, et al. Dinov2: Learning robust visual features without supervision. *arXiv preprint arXiv:2304.07193*, 2023. 2, 4, 8, 12
- [31] Songyou Peng, Michael Niemeyer, Lars Mescheder, Marc Pollefeys, and Andreas Geiger. Convolutional occupancy networks. In *Computer Vision—ECCV 2020: 16th European Conference, Glasgow, UK, August 23–28, 2020, Proceedings, Part III 16*, pages 523–540. Springer, 2020. 5, 6, 7
- [32] Aditya Ramesh, Prafulla Dhariwal, Alex Nichol, Casey Chu, and Mark Chen. Hierarchical text-conditional image generation with clip latents. *arXiv preprint arXiv:2204.06125*, 1(2):3, 2022. 2
- [33] Yuchen Rao, Yinyu Nie, and Angela Dai. Patchcomplete: Learning multi-resolution patch priors for 3d shape completion on unseen categories. *Advances in Neural Information Processing Systems*, 35:34436–34450, 2022. 2, 5, 6, 7, 12
- [34] Ali Razavi, Aaron Van den Oord, and Oriol Vinyals. Generating diverse high-fidelity images with vq-vae-2. *Advances in neural information processing systems*, 32, 2019. 3, 8
- [35] Robin Rombach, Andreas Blattmann, Dominik Lorenz, Patrick Esser, and Björn Ommer. High-resolution image synthesis with latent diffusion models. In *Proceedings of the IEEE/CVF conference on computer vision and pattern recognition*, pages 10684–10695, 2022. 2, 3
- [36] Edward J Smith and David Meger. Improved adversarial systems for 3d object generation and reconstruction. In *Conference on Robot Learning*, pages 87–96. PMLR, 2017. 2
- [37] Jascha Sohl-Dickstein, Eric Weiss, Niru Maheswaranathan, and Surya Ganguli. Deep unsupervised learning using nonequilibrium thermodynamics. In *International conference on machine learning*, pages 2256–2265. PMLR, 2015. 2, 3
- [38] Vignesh Ram Somnath, Matteo Pariset, Ya-Ping Hsieh, Maria Rodriguez Martinez, Andreas Krause, and Charlotte Bunne. Aligned diffusion schrödinger bridges. In *Uncertainty in Artificial Intelligence*, pages 1985–1995. PMLR, 2023. 3
- [39] Yang Song, Jascha Sohl-Dickstein, Diederik P Kingma, Abhishek Kumar, Stefano Ermon, and Ben Poole. Score-based generative modeling through stochastic differential equations. *arXiv preprint arXiv:2011.13456*, 2020. 3
- [40] David Stutz and Andreas Geiger. Learning 3d shape completion under weak supervision. *International Journal of Computer Vision*, 128:1162–1181, 2020. 2
- [41] Arash Vahdat, Francis Williams, Zan Gojcic, Or Litany, Sanja Fidler, Karsten Kreis, et al. Lion: Latent point diffusion models for 3d shape generation. *Advances in Neural Information Processing Systems*, 35:10021–10039, 2022. 3
- [42] Aaron Van Den Oord, Oriol Vinyals, et al. Neural discrete representation learning. *Advances in neural information processing systems*, 30, 2017. 2, 3, 8
- [43] Mathias Vogel, Keisuke Tateno, Marc Pollefeys, Federico Tombari, Marie-Julie Rakotosaona, and Francis Engelmann. P2p-bridge: Diffusion bridges for 3d point cloud denoising. In *European Conference on Computer Vision*, pages 184–201. Springer, 2024. 3, 4, 5
- [44] Bram Wallace and Bharath Hariharan. Few-shot generalization for single-image 3d reconstruction via priors. In *Proceedings of the IEEE/CVF international conference on computer vision*, pages 3818–3827, 2019. 7
- [45] Rundui Wu, Xuelin Chen, Yixin Zhuang, and Baoquan Chen. Multimodal shape completion via conditional generative adversarial networks. In *Computer Vision—ECCV 2020: 16th European Conference, Glasgow, UK, August 23–28, 2020, Proceedings, Part IV 16*, pages 281–296. Springer, 2020. 2, 3
- [46] Xingguang Yan, Liqiang Lin, Niloy J Mitra, Dani Lischinski, Daniel Cohen-Or, and Hui Huang. Shapeformer: Transformer-based shape completion via sparse representation. In *Proceedings of the IEEE/CVF Conference on Computer Vision and Pattern Recognition*, pages 6239–6249, 2022. 2, 3, 5, 6
- [47] X Yu, Y Rao, Z Wang, J Lu, and J Zhou. Adapointr: Diverse point cloud completion with adaptive geometry-aware transformers. *arxiv. arXiv preprint arXiv:2301.04545*, 10, 2022. 14, 15
- [48] Dongsu Zhang, Changwoon Choi, Inbum Park, and Young Min Kim. Probabilistic implicit scene completion. *arXiv preprint arXiv:2204.01264*, 2022. 5, 6
- [49] Junzhe Zhang, Xinyi Chen, Zhongang Cai, Liang Pan, Haiyu Zhao, Shuai Yi, Chai Kiat Yeo, Bo Dai, and Chen Change Loy. Unsupervised 3d shape completion through gan inversion. In *Proceedings of the IEEE/CVF Conference on Computer Vision and Pattern Recognition*, pages 1768–1777, 2021. 2
- [50] Xinyang Zheng, Yang Liu, Pengshuai Wang, and Xin Tong. Sdf-stylegan: Implicit sdf-based stylegan for 3d shape generation. In *Computer Graphics Forum*, pages 52–63. Wiley Online Library, 2022. 5, 6
- [51] Linqi Zhou, Yilun Du, and Jiajun Wu. 3d shape generation and completion through point-voxel diffusion. In *Proceedings of the IEEE/CVF international conference on computer vision*, pages 5826–5835, 2021. 3

- [52] Michael Zollhöfer, Patrick Stotko, Andreas Görlitz, Christian Theobalt, Matthias Nießner, Reinhard Klein, and Andreas Kolb. State of the art on 3d reconstruction with rgb-d cameras. In *Computer graphics forum*, pages 625–652. Wiley Online Library, 2018. [2](#)

Appendix

In this supplementary material, we provide additional details to complement the main manuscript. Specifically, we begin by describing the implementation details, including a in-depth overview of the model architecture and the process of multi-view depth maps. Next, we present a series of additional experiments to further analyze our method. Furthermore, we offer both quantitative and qualitative results to provide a more comprehensive understanding of its performance. Finally, we discuss several failure cases and the limitations of our approach. *Unless otherwise specified, all 3D-EPN results are reported at a 32^3 voxel resolution.*

A. Implementation Details

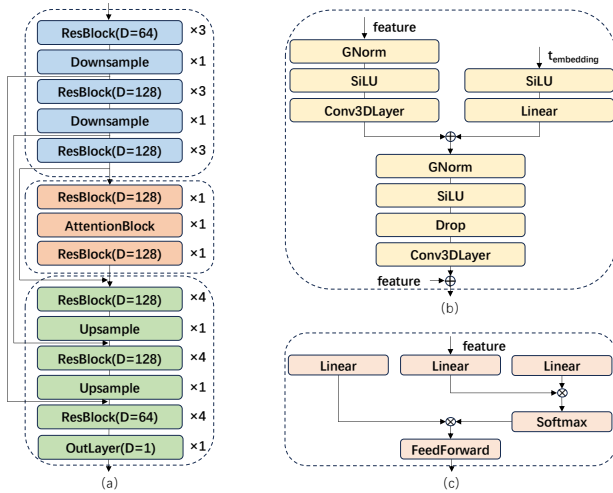


Figure 5. (a) Architecture of the diffusion model, consisting of an encoder, intermediate blocks, and a decoder. (b) Detailed structure of the ResBlock. (c) Detailed structure of the AttentionBlock.

A.1. Model Architecture Details

Figure 5 (a) presents the detailed architecture of our diffusion model, which consists of an encoder, intermediate blocks, and a decoder. The encoder is composed of multiple ResBlock layers and downsampling layers, which reduce the resolution by half at each step. The intermediate block combines two ResBlocks with an AttentionBlock for feature refinement. The decoder reconstructs the spatial dimensions using a mirrored architecture, employing upsampling layers (with a $2\times$ resolution scaling) in conjunction with ResBlocks. Skip connections are used to establish direct pathways between corresponding encoder and decoder stages, ensuring effective information flow. Figure 5 (b) illustrates the detailed structure of the ResBlock, which receives features from the previous layer and a time embedding as inputs. Figure 5 (c) shows the detailed structure of the AttentionBlock.

Table 7. Component ablation: l_1 error at 64^3 and 128^3 .

| Variant | VQ-VAE | DSB | Conv.Diff. | 64^3 | 128^3 |
|---------|--------|-----|------------|--------------|--------------|
| (a) | | ✓ | | 0.047 | 0.045 |
| (b) | ✓ | | ✓ | 0.047 | 0.046 |
| (c) | ✓ | ✓ | | 0.037 | 0.036 |
| (d) | | | ✓ | 0.052 | – |

Table 8. Inference cost and runtime comparison (batch size 1).

| Method | Steps (\downarrow) | GFLOPs/step (\downarrow) | Runtime (s) (\downarrow) |
|-------------------|------------------------|------------------------------|------------------------------|
| DiffComplete | 100 | 159.5 | 3.2 |
| BridgeShape(Ours) | 3 | 33.6 | 0.04 |

A.2. Experiment and training settings

We begin by converting the TUDF data into meshes using the Marching Cubes algorithm [24]. Next, these meshes are projected from 3 different viewpoints using Blender to generate 3 depth maps per shape. These depth maps serve as input for training our Depth-Enhanced VQ-VAE model on complete 3D shapes for 400k steps. During this stage, the DINOv2 [30] model remains frozen, leveraging its pre-trained weights for feature extraction. Initially, we remove the cross-attention layer and train the model solely on complete shapes without depth information. Once the model stabilizes, we incorporate the cross-attention layer and fuse multi-view depth features to enrich the latent space representation, enhancing the model’s ability to capture geometric details from multiple perspectives. Next, we train our diffusion bridge model along with an additional encoder for another 200k steps. For optimization, we use the Adam optimizer [18] with a learning rate of 1×10^{-4} and batch size 16 to train the Depth-Enhanced VQ-VAE, whose latent code $z \in \mathbb{R}^{16^3 \times 3}$ employs a codebook of 8192 entries. For the latent diffusion Schrödinger bridge, we follow prior works—drift $f := 0$, symmetric noise schedule over $T = 1000$ steps—and adopt AdamW [25] at 2×10^{-4} with batch size 24. We inject Gaussian noise into the latent distribution of incomplete shapes before constructing the optimal transport process at a scale of $1\times$. All experiments are conducted on a single RTX 4090 GPU with 24GB VRAM. For the 3D-EPN benchmark [15], we train category-specific models, while on PatchComplete benchmark [33], a unified model is trained across all categories to promote generalization. During inference, we set 3 denoising steps for the diffusion process.

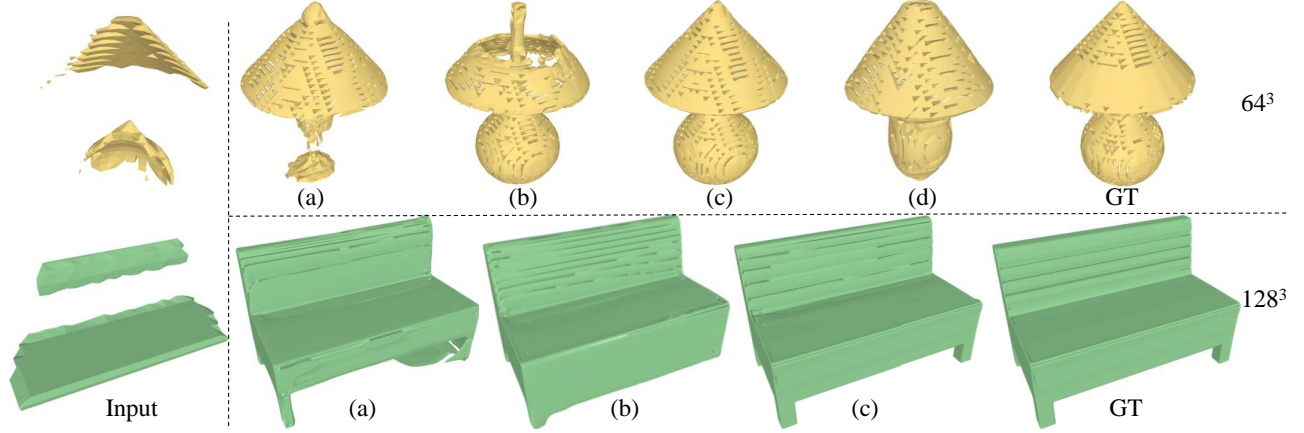


Figure 6. Visuals: Component ablation.

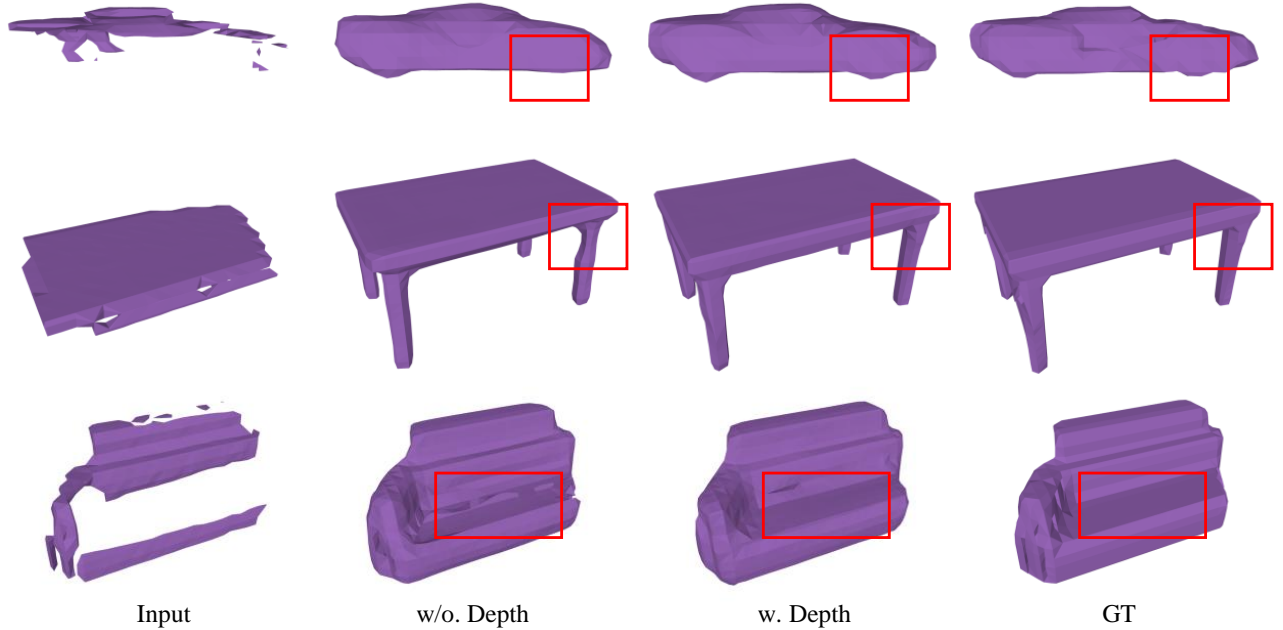


Figure 7. Effect of depth on completion performance.

Table 9. Ablation study on the effect of different feature aggregation strategies.

| Strategies | l_1 -err. (\downarrow) | Memory (GB) (\downarrow) |
|------------------------|------------------------------|------------------------------|
| Concatenation | 0.0553 | 19.60 |
| Max Pooling | 0.0558 | 16.28 |
| Average Pooling (Ours) | 0.0554 | 16.28 |

B. Additional Experiments

B.1. Component Ablation Study

To assess the individual contributions of each module in BridgeShape, we conduct a series of ablation experiments

on 3D-EPN [15] at voxel resolutions of 64^3 and 128^3 . As summarized in Table 7, we evaluate the following variants:

- Voxel-space diffusion Schrödinger(DSB):** Apply the diffusion Schrödinger bridge directly in the original voxel grid, without latent compression.
- Depth-Enhanced VQ-VAE + standard diffusion:** Use our Depth-Enhanced VQ-VAE to encode shapes into latent space, then perform conventional conditional diffusion without the diffusion bridge.
- BridgeShape (ours):** Combine the Depth-Enhanced VQ-VAE with the latent diffusion Schrödinger Bridge.
- Voxel-space standard diffusion:** A baseline using conventional diffusion directly in voxel space (as in Diff-

Table 10. Effect of different numbers of depth views.

| Variants | l_1 -err. (\downarrow) |
|----------------|------------------------------|
| 0 Views | 0.0563 |
| 1 View | 0.0558 |
| 3 Views (Ours) | 0.0551 |
| 6 Views | 0.0551 |

Complete [12]).

Combining the Depth-Enhanced VQ-VAE with standard diffusion (b) reduces the l_1 error from 0.052 to 0.047, highlighting the benefit of a compact yet structurally informative latent space. Using DSB in voxel space (a) yields a similar l_1 error of 0.047. Our full model (c) further lowers the error to 0.037 at 64^3 and 0.036 at 128^3 , demonstrating the synergistic benefit of combining both components. Figure 6 shows side-by-side qualitative comparisons.

B.2. Inference Cost and Runtime Comparison

In addition to superior completion accuracy, BridgeShape offers a dramatic improvement in inference efficiency (see Table 8). BridgeShape requires only three reverse-diffusion steps rather than the hundreds typical of standard noise-to-data models. At 32^3 input resolution and batch size 1, each inference step costs approximately 33.6 GFLOPs, for a total of ~ 100.8 GFLOPs, and the full inference process (encoding, 3 reverse steps, and decoding) completes in just 0.04 s. By contrast, DiffComplete [12] performs 100 diffusion steps at 159.5 GFLOPs each ($\sim 15\,950$ GFLOPs total), requiring 3.2 s per sample—over $80\times$ slower.

B.3. Effects of View Aggregation Mechanism

To assess the influence of different multi-view depth feature aggregation strategies in VQ-VAE, we conduct an ablation study on 3D-EPN [15] chair class, with the results summarized in Table 9. We evaluate three feature aggregation strategies along the view dimension: average pooling, concatenation, and max pooling. The study investigates both the final completion performance and GPU memory consumption during VQ-VAE training, with GPU memory usage reported for a batch size of 12. Our results show that average pooling achieves a comparable l_1 -error to concatenation, while significantly reducing memory consumption. In contrast, max pooling leads to a slight drop in accuracy, likely due to its tendency to retain only the most dominant responses, discarding fine-grained geometric details. These findings suggest that average pooling effectively captures complementary information across views while maintaining computational efficiency, making it a well-balanced choice for feature aggregation.

Table 11. Effect of noise scale.

| Noise Scale | l_1 -err. (\downarrow) |
|-----------------------------|------------------------------|
| 0.5 \times | 0.043 |
| 1\times | 0.039 |
| 2 \times | 0.044 |

Table 12. Effect of codebook size.

| Size | Rec. l_1 \downarrow | Comp. l_1 \downarrow | Comp. IoU \uparrow | Time (norm.) \downarrow |
|-------------|-------------------------|--------------------------|----------------------|--------------------------------|
| 4096 | 0.0034 | 0.040 | 92.23% | 1.00\times |
| 8192 (ours) | 0.0021 | 0.039 | 94.41% | 1.07 \times |
| 16384 | 0.0022 | 0.039 | 94.37% | 1.12 \times |

Table 13. Comparison with point cloud completion approach. (ℓ^1 CD $\times 10^3$ and F1-Score@1%)

| Methods | CD (\downarrow) | F1 (\uparrow) |
|--------------------|---------------------|-------------------|
| AdaPoinTr [47] | 21.52 | 0.286 |
| BridgeShape (Ours) | 15.60 | 0.518 |

B.4. Ablation on the number of projections

Table 10 provides a quantitative evaluation of the effect of incorporating different numbers of depth views (0, 1, 3, and 6 views) on the 3D-EPN [15] chair class. The results show that increasing the number of depth views consistently improves completion accuracy. Notably, the performance plateaus after 3 views, indicating that additional views beyond this threshold do not yield significant improvements. Based on this observation, we select 3 views for the experimental configuration, as it strikes an optimal balance between enhanced accuracy and computational efficiency.

B.5. Ablation on the Scale of Stochasticity

We evaluate the impact of Gaussian noise scale injected into the latent distribution of incomplete shapes on final completion performance on 3D-EPN [15]. As shown in Table 11, a scale of $1\times$ achieves the lowest l_1 error, confirming that this level of stochasticity most effectively stabilizes the optimal transport process and compensates for missing geometry.

B.6. Ablation on the Size of the Codebook

To evaluate the impact of codebook capacity on representation quality and completion cost, we compare three sizes (Table 12). While larger sizes offer only marginal gains in VQ-VAE’s reconstruction fidelity and final completion accuracy, they incur higher inference cost—making 8192 the best trade-off.

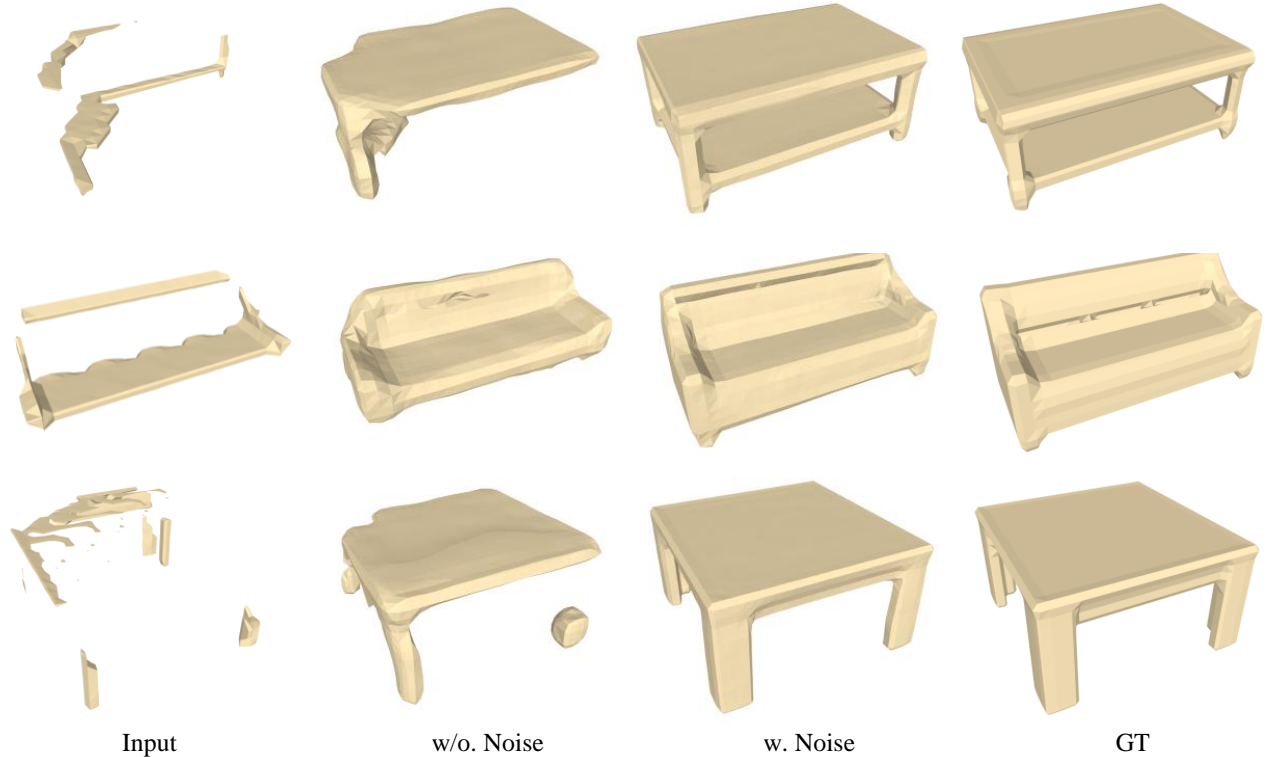


Figure 8. Effect of stochasticity on completion performance.

B.7. Comparison with Point Cloud Completion Approach

We compare our method with the state-of-the-art AdaPoinTr [47] in the task of point cloud completion on 3D-EPN [15] chair class. For fair comparison, we adopt the experimental settings commonly used by AdaPoinTr, where 2048 points are sampled from the incomplete shape surface and 8192 points from the complete shape surface for training AdaPoinTr. To ensure consistency in evaluation, we sample 8192 points from our predicted shape. We report the ℓ^1 version of Chamfer Distance (CD) and F1-Score as evaluation metrics. As shown in Table 13, our method achieves significantly improved completion performance. This result underscores the effectiveness of our approach.

C. More Quantitative Visualizations

C.1. Effect of Depth on Completion Performance

Figure 7 provides qualitative results of the impact of incorporating self-projected multi-view depth information on shape completion results. The figure demonstrates that using multi-view depth maps improves geometric consistency and the recovery of fine-grained details—for example, for example, in the completion of car tire, chair leg, and sofa surface.

C.2. Effect of Stochasticity on Completion Performance

Figure 8 presents qualitative results illustrating the impact of injecting stochasticity into the latent distribution of incomplete shapes before constructing the optimal transport process. The figure highlights that this design is particularly effective in handling extremely sparse incomplete shapes, where significant uncertainty in the missing regions can hinder the establishment of a robust optimal transport path, thereby reducing completion accuracy.

C.3. Fine-Grained Visualization Comparisons

Figure 10 compares BridgeShape against DiffComplete on 3D-EPN [15] at both 32^3 and 64^3 resolutions. BridgeShape delivers more accurate hole filling, sharper recovery of fine geometry, and stronger global completeness—benefits that are even more pronounced at the higher 64^3 resolution.

C.4. Visualizations on Known Object Categories

Figure 11 displays qualitative results comparing the state-of-the-art DiffComplete [12] with our BridgeShape across different known object categories. As shown, our method produces shape completions that are more realistic and visually coherent. Furthermore, our completions are highly accurate, closely aligning with the ground truth shapes.

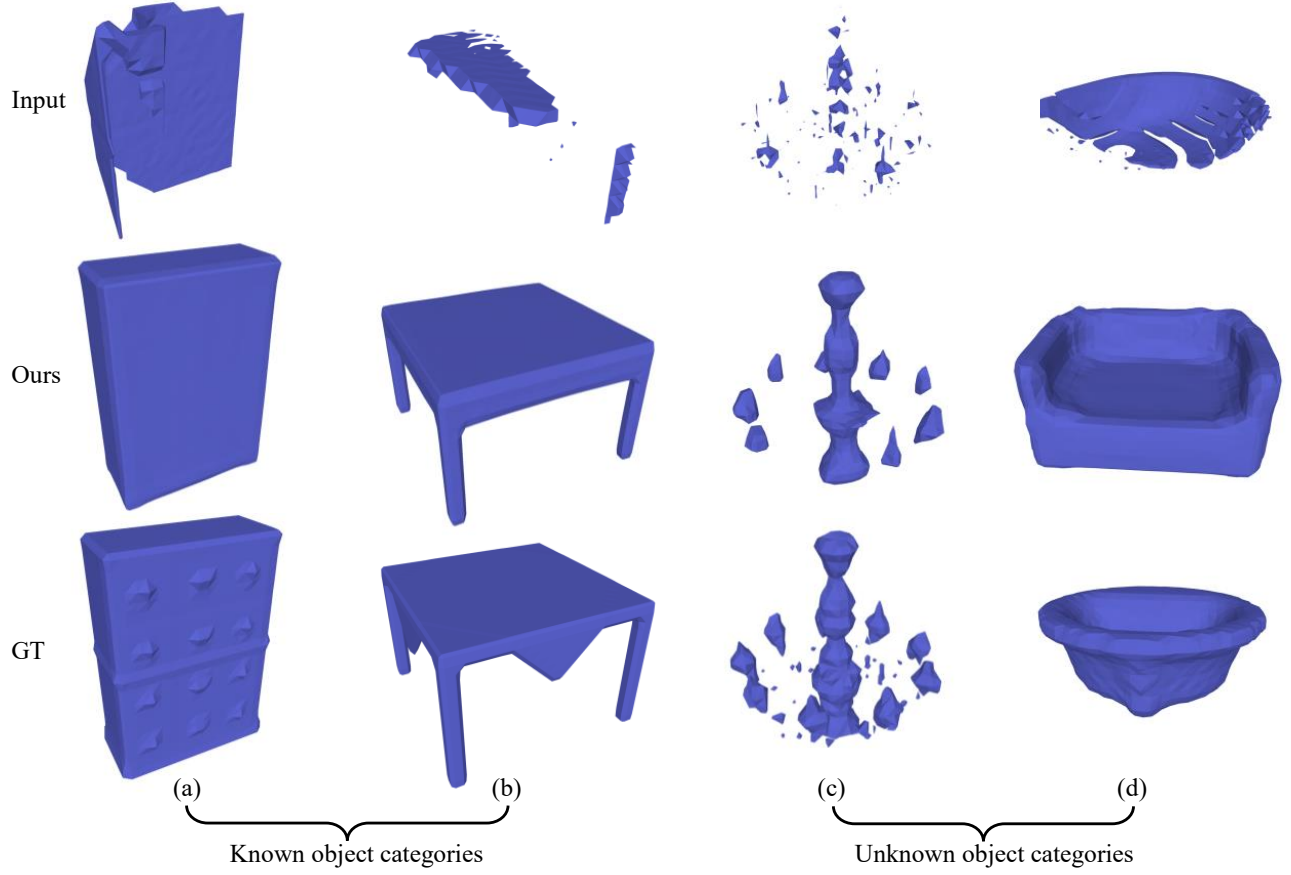


Figure 9. Example of failure cases.

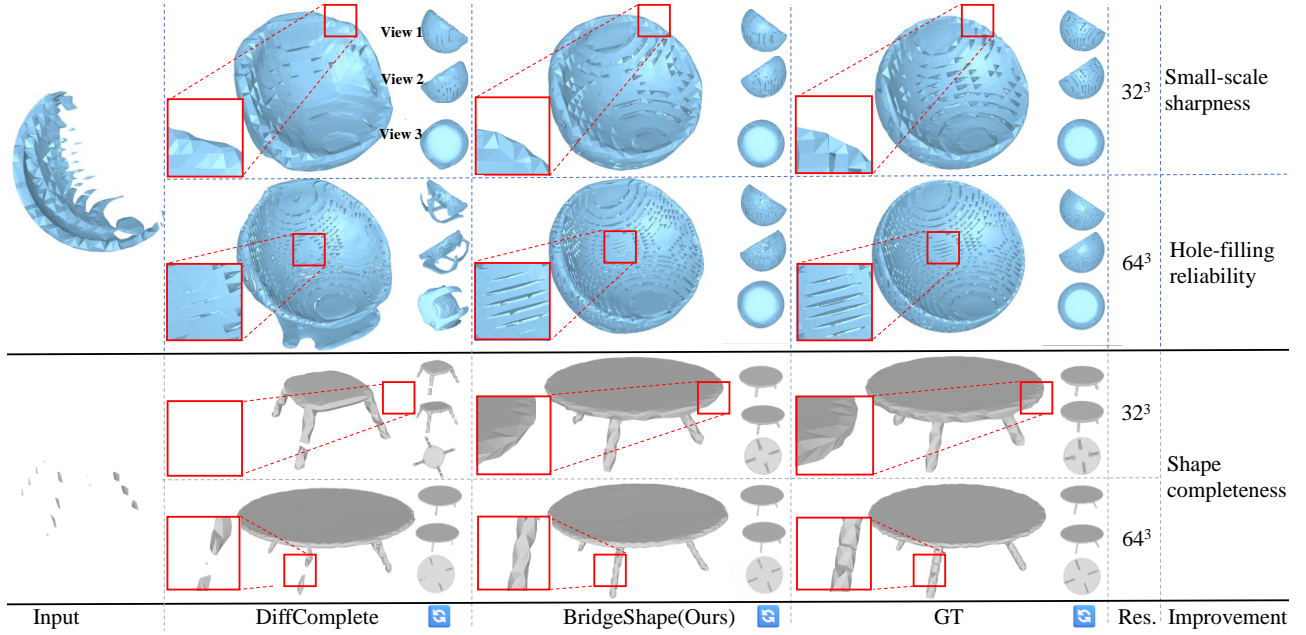


Figure 10. BridgeShape vs. DiffComplete [12] at 32^3 and 64^3 .

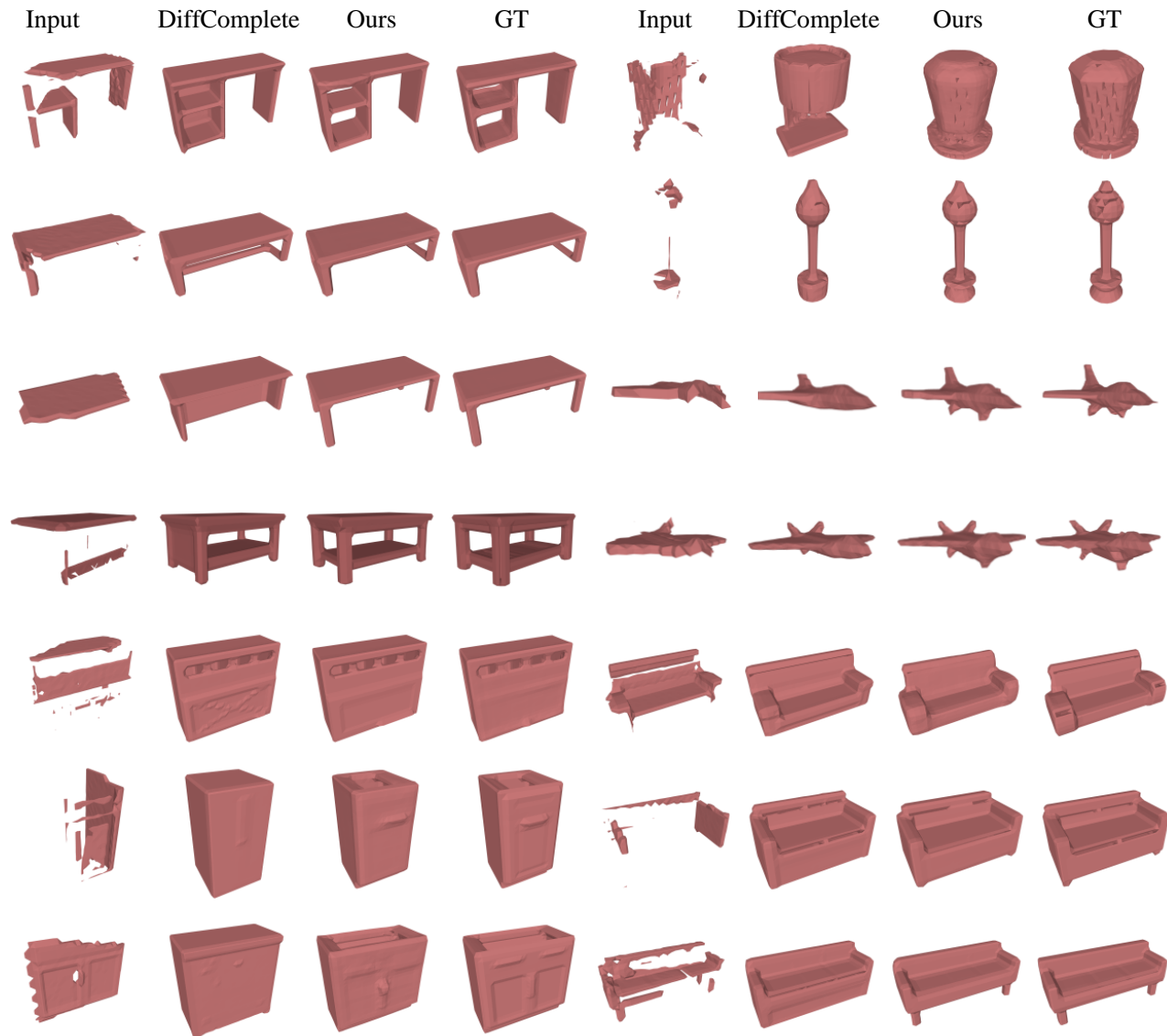


Figure 11. Visual comparison with DiffComplete [12] on 3D-EPN [15].

C.5. Visualizations on Unseen Object Categories

As shown in Figure 12 and Figure 13, when applied to unseen object categories, our method outperforms DiffComplete [12] in terms of both global consistency and local detail preservation. This demonstrates our method’s strong generalization capability, even when faced with real-world objects.

D. Failure Cases and Limitations

Although our method demonstrates promising results in 3D shape completion, several failure cases and inherent limitations indicate areas for further improvement. Figure 9 presents several failure cases of our method. For known

object categories (examples a and b), when the input is extremely sparse, the model sometimes fails to recover subtle geometric details—even though we introduce stochasticity to mitigate such cases—for instance, the intricate textures on cabinet surfaces. For unknown categories (examples c and d), the challenges are even more pronounced. In example (c), the model struggles to complete complex, cluttered lamp pendant structures, while in example (d), it erroneously predicts a sofa shape, despite the ground truth being a container. Overall, these failures highlight two key weaknesses: (1) the inability to complete fine details under extreme sparsity, and (2) limited generalization to highly diverse or irregular shapes. Beyond these challenges, our method also faces broader limitations related to latent space

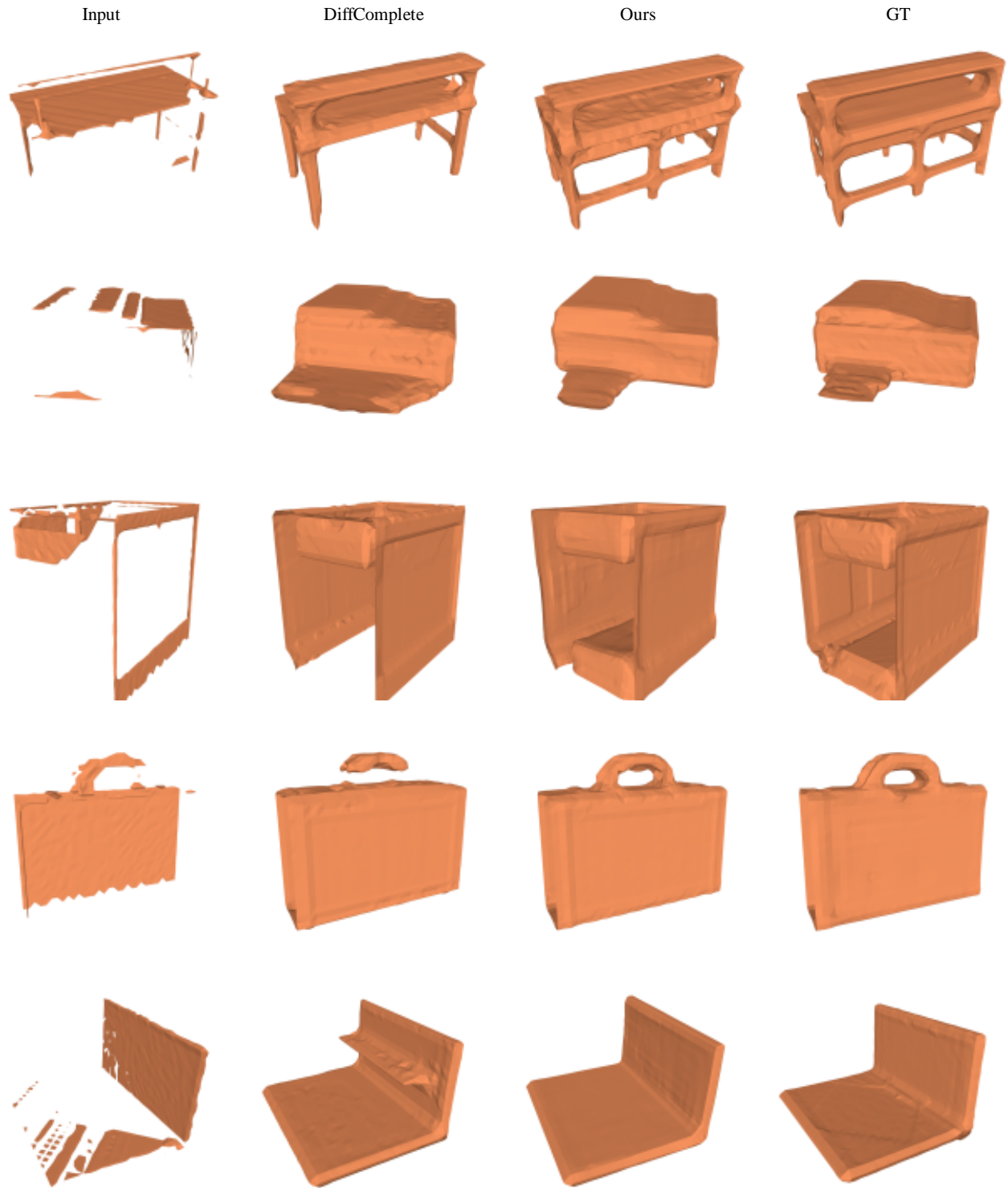


Figure 12. Visual comparison with DiffComplete [12] on Shapenet [4].

representation and computational efficiency.

Specifically, the reliance on a pre-trained VQ-VAE for

latent encoding may hinder generalization to highly complex or noisy 3D shapes with intricate topologies. Addition-

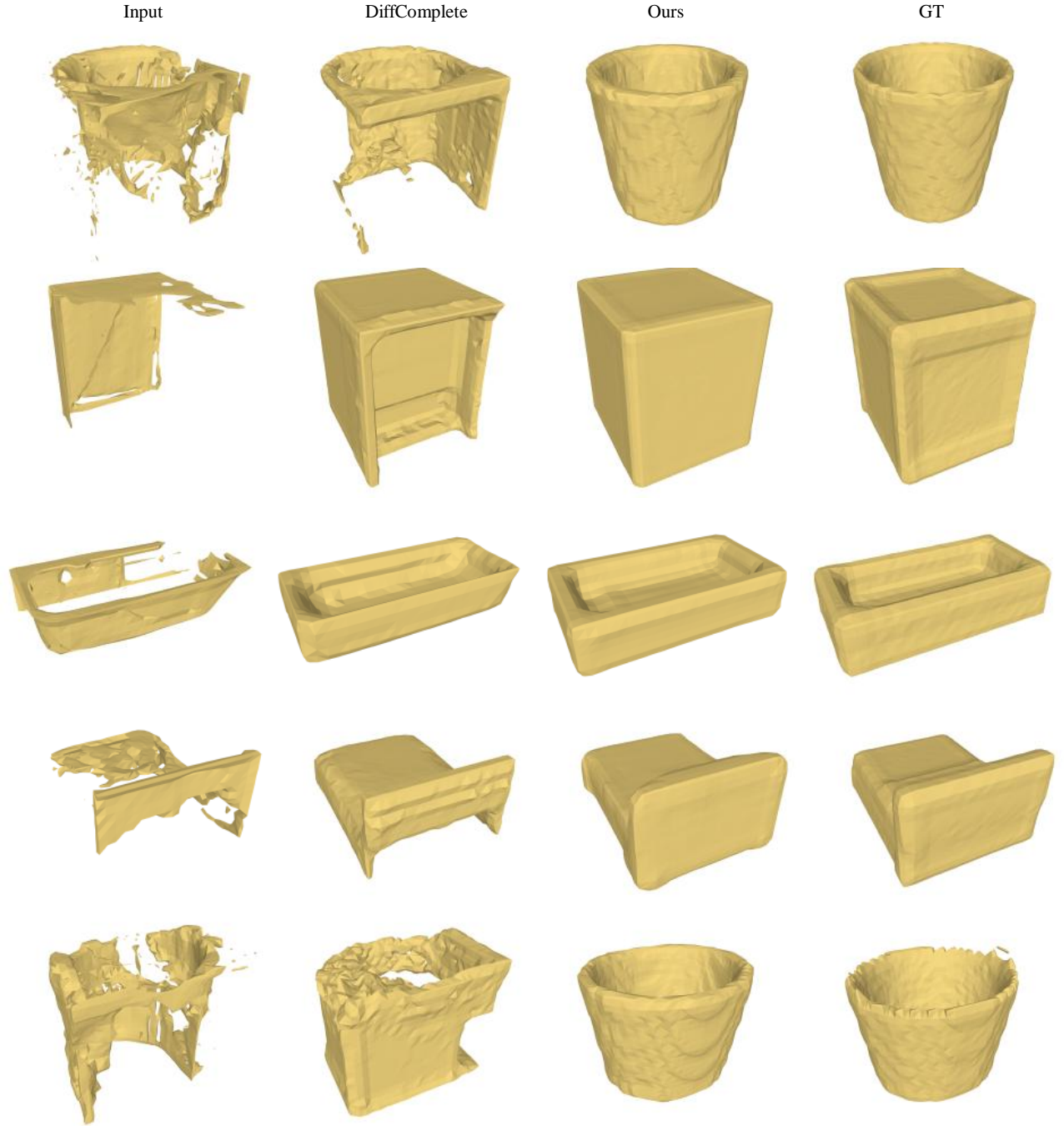


Figure 13. Visual comparison with DiffComplete [12] on Scannet [14].

ally, the use of multi-view depth maps introduces computational and memory overhead, potentially limiting scalability in large-scale or real-time applications. Addressing these limitations in future work could involve exploring adaptive sparsity-aware mechanisms, refining latent representations through joint training strategies, or exploring more efficient self-projected multi-view depth fusion techniques to reduce

computational overhead while maintaining accuracy.